PCCP

ROYAL SOCIETY OF CHEMISTRY

www.rsc.org/pccp

Effect of Structural Dimensionality on the Electrocatalytic Properties of Nickel Selenide Phase

Suresh Kukunuri, M Reshma Krishnan and S Sampath*
Department of Inorganic and Physical Chemistry
Indian Institute of Science, Bangalore 560012, India

Abstract

Nickel selenide (NiSe) nanostructures possessing different morphologies of wires, spheres and hexagons are synthesized by varying the selenium precursors, selenourea, selenium dioxide (SeO_2) and potassium selenocyanate (KSeCN) respectively and are characterized using X-ray diffraction, X-ray photoelectron spectroscopy, Raman spectroscoscopy, transmission electron microscopy and scanning electron microscopy techniques. Electrical measurements of single nanowire and hexagon carried out on devices fabricated by focused ion beam (FIB) technique depict the semiconducting nature of NiSe and its ability to act as visible light photodetector. The three different morphologies are used as catalysts for hydrogen evolution (HER), oxygen reduction (ORR) and glucose oxidation reactions. The wire morphology is found to be better than that of spheres and hexagons for all the reactions. Among the reactions studied, NiSe is found to be good for HER and glucose oxidation while ORR seems to terminate at the peroxide stage.

1. Introduction

Development of materials for efficient energy conversion has been in the fore front of research for several years.[1-4] Among the known materials, transition metals such as platinum and palladium have been shown to possess very good electrocatalytic activity towards various reactions of interest such as electrooxidation of formic acid, hydrogen oxidation, oxygen reduction and oxidation of small molecules such as methanol, ethanol, ethylene glycol, and glycerol.[5-12] The electrocatalytic activity has been correlated to the d-band states (DOS) at the Fermi level.[13,14] Higher the DOS, higher is the electrocatalytic activity of the element. Platinum and palladium have favourable DOS at Fermi level and these metals tend to show good electrocatalytic activities for most of the reactions. Additionally conductivity and stability are other favourable parameters. In addition to pure metallic Pt and Pd, their alloys also show good activities towards most of the reactions. For example Noto et al. have reported $PtNi_x$, PdCoNi alloys for improving the electrocatalytic activities towards oxygen reduction reaction.[15,16] In this direction, transition metal chalcogenides offer themselves as good candidates.[17] Metallic Ir, Ru, Pd and some of their selenides are reported to be good catalysts for reactions such as hydrogen evolution (HER) and oxygen reduction (ORR).[18-21] Use of earth abundant and inexpensive binary metal (Co, Mo, Cu, Ti and W) sulfides, nitrides, borides, and phosphides have also been reported.[22-26] Natural systems containing hydrogenase enzymes possessing metal sulfur clusters with five permanent ligands in distorted octahedral environment have been proved to be effective for HER.[27] The active site contains either Fe, Ni or both. There have been several efforts to synthesize inorganic metal sulfur complexes and solids to mimic the active site of the enzyme.[28] Analogous to hydrogenases, FeS_2 and NiS_2-based materials have also been reported as good HER catalysts.[29,30] Activity of other metal chalcogenides such as CoS_2, MoS_2, $MoSe_2$, WS_2, $CoSe_2$, $CuSe_2$, and FeSe and their alloys have been reported for reactions such as HER, ORR and also as electrodes for solar cells, supercapacitors, and batteries.[25,31-38] Analogues nickel sulfides such as NiS, NiS_2, Ni_3S_2 and Ni_3S_4 phases have been studied as well.[39-43] In a different direction, Ni_3S_2 nanoparticles are shown to exhibit high electrocatalytic activity toward glucose oxidation. The performance of glucose sensor based on Ni_3S_2/MWCNT-NC is examined by cyclic voltammetry (CV) and amperometric methods revealing high sensitivity and good linear dependence on glucose concentration, and selectivity to glucose.[44-46]

The electronegativity difference between nickel and selenium is small and they can form different phases, including non-stoichiometric compounds. Based on the phase diagram, Ni forms very stable NiSe, $NiSe_2$ and Ni_3Se_2 phases under ambient conditions. Synthesis of various metal selenides have been reported using methods[40,47-55] such as solid-state reaction at high temperatures, magnetron sputtering, mechanical alloying, sonochemical method and chemical vapour deposition. Many of these methods usually require stringent conditions including high temperatures, high pressures or use of inert atmosphere. Another frequently used method involves the reaction of the NaHSe, H_2Se, selenium powder and metal or its compounds.[56] There have also been reports on the use of hydrothermal synthesis method [48,54] where moderate temperatures of ~ 180°C have been used. Ni_3Se_2 phase has been reported for photocatalytic water splitting, though the activity is relatively moderate.[57]

The low dimensionality of nanostructures lead to superior physicochemical properties as compared to their bulk counter parts.[58-60] As for the NiSe phase, Yu et al.[61] have reported the preparation of sea-urchin morphology - like nanostructures by hydrothermal method and further studied their photoluminescence properties. Wang et al.[62] have reported transparent thin films of $Ni_{0.85}Se$ and $Co_{0.85}Se$ on FTO plates and used them as counter electrodes in

DSSCs. The preparation of these nanostructures involves either high temperatures or prolonged reaction times.

In the present study, preparation of NiSe nanostructures of different morphologies such as wires, hexagons and spheres has been achieved using different selenium precursors of selenourea, KSeCN and SeO_2 respectively. The electrical properties of single NiSe wires and hexagons and the dependence of resistivity on temperature have been followed. The electrocatalytic properties of NiSe have not been reported so far and the present study explores this aspect towards HER, ORR and glucose electrooxidation reactions.

2. Experimental section

2.1 Chemicals

All the chemical reagents used were of analytical grade and were utilized without any further purification. Nickel chloride ($NiCl_2.6H_2O$), selenourea [$SeC(NH_2)_2$], selenium dioxide (SeO_2), potassium selenocyanate (KSeCN), hydrazine hydrate ($N_2H_4.H_2O$), glucose, ascorbic acid, uric acid and ethylenediaminetetraacetic acid (EDTA) were procured from Aldrich, USA. Sodium hydroxide (NaOH), acetone, ethanol and iso-propanol are obtained from Polysales, India. De-ionized water (resistivity 18 MΩ.cm) was used for all the experiments.

2.2 Synthesis of nanostructures of NiSe

Different morphologies of NiSe were prepared using various selenium precursors under identical conditions. $NiCl_2.6H_2O$ and selenium precursor (selenourea/ selenium dioxide/ potassium selenocyanate) in the molar ratio, 1:3 was used and a typical synthesis involved the following procedure. Calculated amount of $NiCl_2.6H_2O$ (100mg, 0.42 mmoles) was added into 12 mL of deionized water with continuous stirring. After 10 minutes, the chelating agent, EDTA (500 mg, 0.0013 moles), was added to the solution and the solution pH was adjusted to 14 by adding NaOH (500 mg, 0.012 moles). Hydrazine hydrate (4 mL) was subsequently added to the above mixture to reduce Ni^{2+} ions. After another 10 minutes of stirring, the selenium precursor (Selenourea, 155 mg, 1.262 mmoles/ SeO_2, 140 mg, 1.262 mmoles/ KSeCN, 182 mg, 1.262 mmoles) was introduced and the resulting mixture was stirred for further 30 minutes. The solution was then transferred to a 20 mL teflon lined autoclave and heated at 180°C for 8h in a furnace. The autoclave was allowed to cool to ambient conditions and the material was collected by centrifuging the colloid at 4000 rpm. The sediment was washed several times with water and ethanol to remove any unreacted hydrazine and selenium precursor.

2.3 Characterization

The as-obtained materials were characterized by various techniques. The X-ray diffraction (XRD) was carried out using a diffractometer (PANalytical, XRD) with Cu-K_α source. The morphology was characterized by field emission scanning electron microscopy (FESEM, Carl Zeiss ultra 55) and transmission electron microscopy (TEM, JEOL 2100F/FEI Tecnai 200 kV). Energy dispersive X-ray spectra (EDS) and elemental mapping were carried out in scanning (STEM) mode. The sample for TEM studies was prepared by drop casting ethanol dispersions of NiSe onto carbon coated copper/holey carbon grid. X-ray photoelectron spectroscopic analysis was performed on a Kratos Axis Ultra DLD X-ray photoelectron spectrometer with monochromatic Al kα excitation (1486.7 eV) radiation. Raman spectroscopy was carried out (LabRAM, Horiba Jobin Yvon) at an excitation wavelength of 514 nm and 50x long working distance objective. Electrical measurements were recorded using a Keithley 4200 SCS workstation combined with a probe station (Everbeing, Taiwan) equipped with a thermal chuck.

2.4 Electrochemical studies

All the electrochemical measurements were performed in a conventional three electrode assembly using potentiostat/galvanostat (660A, CH Instruments. USA). The nickel selenide (NiSe) catalyst was coated on a glassy carbon electrode (diameter of 3 mm) and used as the working electrode (WE) and a large platinum foil as the counter electrode. Reference electrodes used in acidic and alkaline media were saturated calomel electrode (SCE) and mercury/mercuric oxide (Hg/HgO) electrode respectively. The working electrode was fabricated as follows. A known amount of the catalyst and 10µL of 5 wt.% nafion (a mixture of lower aliphatic alcohols and H_2O) were dispersed in 1mL of 4:1 v/v water/iso-propanol mixture to get a homogeneous ink. 10 µL aliquot of the catalyst ink was transferred onto a GC electrode by drop casting to achieve a loading of ~ 0.570 mg/cm^2. The electrolytes used for HER and ORR studies were 0.5M H_2SO_4 and 0.1 mol L^{-1} KOH respectively. Prior to the electrochemical measurements, the electrolyte was de-aerated by continuously purging with high purity N_2 gas for 30 minutes. The stability of the catalysts was determined by cyclic voltammetry (CV) at a scan rate of 100 mV s^{-1} for 1000 cycles. The electrochemical impedance spectra (EIS) were recorded in the frequency range of 100 KHz to 0.05 Hz with AC amplitude of 5 mV. The reference electrodes were calibrated against reversible hydrogen electrode using an already known procedure.[52] In 0.5 mol L^{-1} H_2SO_4, E (RHE) = E (SCE) + 0.265 V (Fig. S1). The calibration of Hg/HgO electrode in 0.1 mol L^{-1} KOH was also carried out at 25°C and E (RHE) = E (Hg/HgO) + 0.928 V (Fig. S2).

2.5 Glucose oxidation

Glucose oxidation experiments were carried out in a three electrode system with NiSe catalyst coated glassy carbon (GC) as the working electrode (WE), a large Pt foil and Hg/HgO (0.1 mol L^{-1} KOH) as auxillary and reference electrode respectively. 0.5 mol L^{-1}

NaOH was used as the electrolyte and it was purged with N_2 before each measurement to remove any interference from dissolved O_2. The current response was evaluated by cyclic voltammetry and constant potential chronoamperometry.

2.6 Electrical measurement

Pt contact pads to a single nanowire and hexagon were achieved using focussed ion beam (FIB) deposition technique (FEI dual beam SEM, operating voltage, 30 KV). The Pt contact pads of defined areas were deposited using 30 KV Ga^+ ions at a current of 80 pA - 9.3 nA depending on the pad dimensions. The thickness of the contact pads was maintained at 800 nm. The I-V measurements were carried out using Keithley 4200 SCS workstation combined with a probe station (Everbeing, Taiwan) and a thermal chuck. Photoresponse measurements were carried out by shinning a red laser (wavelength 630 nm) of 0.6 mW and optical microscope lamp.

3. Results and discussion

Different morphologies of NiSe formed using the three precursors are quite stable and they are black in color. The preparation conditions (8 h duration at 180°C) are optimized based on the fact that pure phase of NiSe with the required morphology is obtained under the conditions used (Fig. S3 and S4). The XRD patterns of NiSe reveal that (Fig. 1) they crystallize in hexagonal system with lattice parameters, a = 3.6 Å and c = 5.3 Å. The obtained patterns match well with the standard pattern (JCPDF 18-0888). The average crystallite size calculated using Scherrer formula are 319, 331 and 344 Å (± 5Å) for wires, spheres and hexagons respectively.

The macroscopic morphologies of NiSe phase obtained vary as spheres, wires and hexagons when SeO_2, selenourea and KSeCN are used as precursors respectively (Fig. 2).

The morphology of the product obtained at different times of reaction (1, 3, 5 and 8 h) reveals that a minimum of 8 h is required for complete conversion in to wires (Fig. S4). Figure 3 shows the TEM images of NiSe wires, spheres and hexagons. Different crystallographic planes are exposed for different morphologies. The interplanar distance is found to be 2.70, 2.69 and 2.73 Å for nanowires, spheres and hexagons respectively. The d-spacing values correspond to (101) plane in the three morphologies. The selected area electron diffraction (SAED) pattern given in figure 3(g) to (i) show discrete spots in all the three cases, indicating good crystallinity and the elemental analysis (Fig. S5) shows the presence of Ni and Se in the ratio of 1:1, which is in agreement with the phase observed using XRD technique.

The different macroscopic morphologies of NiSe seem to arise from the Se nanostructures formed during the hydrothermal reaction. The morphologies of elemental Se obtained from different precursors (without Ni^{2+} in the reaction mixture) are followed using microscopy. As given in Figure S6, the morphologies of Se formed are predominantly wires and hexagons when selenourea and KSeCN are used as selenium precursors respectively. It is already known that SeO_2 results in Se with spherical morphology.[63]

It has been reported that the selenium precursor, Na_2SeO_3 is quickly reduced to Se upon heating. The elemental Se is converted to Se^{2-} through a disproportionation process in highly alkaline medium.[63-66] Yadong Li et al.[63] have reported that Na_2SeO_3 along with Ni salt under alkaline conditions in the presence of hydrazine results in the formation of spherical NiSe phase. The authors have explained the formation of spheres based on the speculation that amorphous Se formed from the precursor possesses spherical morphology before reacting with Ni^{2+}. The mechanism suggested by the authors[63] involves the reaction of nickel ions interacting with the Se^{2-} (and $2SeO_3^{2-}$) formed from Se. The formation of Se is confirmed to be from the precursor in presence of alkali. Another route suggested by the same group[63] invokes the formation of Ni from Ni^{2+} in presence of hydrazine and subsequent formation of NiSe by reacting with elemental Se.

In the present study, the three morphologies of NiSe are achieved by using different selenium precursors: selenourea, SeO_2 and KSeCN. Selenium precursors are known to get reduced to amorphous selenium in the presence of hydrazine under alkaline conditions at temperatures of ~ 180°C[63] in addition to other by-products. SeO_2 is known form water and N_2 while KSeCN may lead to CN^- containing products such as HCN and N_2. Selenourea on the other hand, may lead to ammonia / ammonium hydroxide and N_2. The Ni^{2+} is also known to get reduced to Ni(0) in presence of hydrazine under alkaline conditions[63] at moderately high temperature. The formation of different morphologies may depend on several factors. (1) The formation of various by-products in presence of different Se precursors as given above. For example, cyanide in the case of KSeCN and ammonia-related species in the case of selenourea. In addition, there may be a change in the pH of the medium due to the by-products formed. (2) Relative rates of amorphous selenium dissolution to Se^{2-} in presence of alkali as opposed to the reaction between Se and metal (0) formed. Hence, it is likely that the NiSe morphology obtained in presence of different Se precursors are dictated by the Se morphology based on the precursors.

The composition of the as-prepared samples is further examined by X-ray photoelectron spectroscopy (XPS). Figure 4 shows the XPS survey spectrum of nanowire morphology and the high resolution data for all the three morphologies. The deconvoluted Ni-2p region shows peaks at binding energies of 855.7 and 874.3 eV corresponding to $2p_{3/2}$ and $2p_{1/2}$ states respectively. Corresponding Se peaks are observed at 53.7 and 54.4 eV for $3d_{5/2}$ and $3d_{3/2}$ levels respectively. The binding energy values are well in agreement with reported values in the literature for NiSe phase.[67] The Raman spectrum of NiSe nanowires show bands around 511, 674 and 1058 cm^{-1}, which correspond to the following vibration modes: longitudinal optical (LO) one-phonon mode, LO two-phonon mode and transverse optical (TO) two-phonon mode respectively. The other peaks observed around 180 and 350 cm^{-1}, may be assigned to Se-Se librational and stretching vibrations or their combination mode as given earlier.[67] Similar peak positions have been observed in the case other two morphologies with varying intensities (Fig. 5). The band observed at 511 cm^{-1} has been assigned to the surface defects present on NiSe.[67] In the present studies, the relative intensities of this band are determined to be 607, 262 and 150 counts for spherical, hexagons and wire-like morphologies respectively. The micrographs (Fig. 2) clearly reveal that the spherical particles are round and composed to small primary particles which will lead to surface defects. The defects on hexagons and wire morphologies are relatively small.

Electrical measurements are carried out on a device fabricated using FIB technique. Inset of figure 6(a) shows the SEM image of the fabricated device consisting of a single nanowire of length 6 μm and diameter of 40 nm. The corresponding I-V plot of a single nanowire device is also given. Linear variation with voltage indicates good ohmic contact between the nanowire and the Pt contact pads. Resistance values are found to be ~ $(1.4 \pm 0.2) \times 10^4\ \Omega$ and $(0.35 \pm 0.05) \times 10^4\ \Omega$ at 0.9 V bias, for wires and hexagons respectively, at 25^oC. The resistivity values are 3.1 and 1840 μΩ.m for wire and hexagon morphologies. This is comparable to the resistance values reported for PbSe[68], Sb_2Se_3[69] and Ag_2Se[70] nanowire morphologies. The resistance values for different morphologies may be different depending on the preparation conditions and probably the doping levels. This will lead to different dark currents for different morphologies.

The resistance value observed for bundle of NiSe wires decreases with increase in temperature indicating that the material is semiconducting in nature [Fig. 6(b)]. Similar observations are made for the hexagons and spherical particles as well. The optical band gap of bulk NiSe film is known to be approximately 1.8 eV[71] while it is found to be ~ 1.9 eV for the wire morphology based on the absorption spectrum. As the band gap lies in the visible region of the electromagnetic spectrum, photoconductivity studies are carried out on the device consisting of individual nanowire. Figure 6(c) illustrates the I-V behavior of the nanowire in the absence and the presence of visible light (of wavelength 450 nm - 750 nm based on the lamp spectrum). There is a significant increase in currents observed when the nanowire is illuminated with the red laser of 0.6 mW. These observations indicate the capability of NiSe nanowires to act as visible light photodetector. The results obtained for hexagon morphology (between patterned Pt contacts) is shown in the inset of figure 6(a). The photocurrents in the case of hexagons are higher than the nanowire sample [Fig. 6(d)]. The bandgap is slightly higher in the case of nanowire (1.9 eV) as compared to hexagon (1.8 eV - size of the flake ~ 6 μm) morphology. However, the relative increase in photocurrent with respect to the dark current is very similar for both morphologies, (0.30±0.3) and (0.27±0.2) for wires and hexagon respectively. The I_{ON} / I_{OFF} ratio is found to be ~1.3 for both the morphologies.

Use of NiSe for electrochemical studies has not yet been explored. The electrocatalytic activity of the three different morphologies of NiSe towards standard Fe (II) / Fe (III) redox system in 0.1 mol L^{-1} KCl solution is shown in figure S7. The nanowire morphology shows good reversible redox peaks as compared to the other two morphologies. Parameters such as peak currents, peak potentials, and peak separation (ΔE) values as deduced from the voltamograms are tabulated in table 1. Linear variation of peak currents with the square root of scan rate indicates diffusion controlled process [Fig. S7]. Other two morphologies also show similar observations (Fig. S8).

Hydrogen evolution

The electrocatalytic activities towards redox reactions, hydrogen evolution (HER) and oxygen reduction (ORR) have been followed and the HER data are shown in figure 7(a). The onset potentials for HER are observed to be -0.22, -0.25 and -0.29 V vs. RHE for wires, spheres and hexagons respectively. The voltage required to achieve a current density of 50 mA/cm^2 is more positive in the case of wires (-0.26 V) than spheres (-0.3 V) which in turn is more positive than hexagons (-0.4 V). The Tafel slopes determined from the slow scan voltammograms are observed to be 52, 98 and 112 mV/decade for wires, hexagons and spheres respectively [Fig. 7(b)]. The HER evolution probably follows Volmer-Heyrovsky mechanism in the case of spheres and hexagons, wherein the electrochemical recombination of hydrogen atom with a proton is the rate-limiting step. The Tafel slope being smaller in the case of wires indicate that Volmer-Tafel may operate along with contributions from spillover mechanism. Among the three morphologies, wires seem to show better kinetics than the other two forms. Possible reasons for the wire morphology showing better activity than the hexagons and spheres are given later. The stability of the electrode material is checked by scanning the potential from -0.2 to -0.7 V vs. SCE for 1000 cycles and it is observed that there is negligible loss of cathodic currents in the case of wires [Fig. 7(c)] again substantiating the fact the wire morphology is very good for electrocatalytic activity. The stability studies related to other two morphologies are given in the supporting information (Fig. S9) and are found to be good. The impedance spectra [Fig. 7(d)] obtained at a potential of -0.235V vs. RHE reveal (Table 2) that the NiSe wires possess the lowest R_{ct} values as compared to the spheres and hexagons. The impedance data are fitted with an equivalent circuit given in the figure 7d.

The relative electrode surface areas are determined using cyclic voltammetry in the non-faradic potential region based on the double layer capacitance as reported earlier for NiS.[44] The difference in current density at a potential of 0 V in the anodic and cathodic regions vary linearly with the scan rate. The straight line enables the extraction of geometric double layer capacitance (C_{dl}), which is proportional to effective electrode surface area. The relative capacitance values for the three different morphologies [Fig. S10(a) to (c)] in the non-faradic region [Fig. S10(d)] of - 0.1 to 0.1 vs. SCE (scan rate of 10 to 100 mV s^{-1}) are 430, 136, and 76 μF for wires, spheres and hexagons respectively with respect to the same mass loading of the material on glassy carbon of the same geometric area. The capacitance of wires is 5 times higher than the hexagons and 3 times higher than the spherical morphology. Higher capacitance values in the case of wires indicate larger accessible surface area and therefore higher number of active sites available for hydrogen adsorption as compared to spheres and hexagons.

Among various parameters that govern the electrocatalytic activity of a particular material with different morphologies, (1) surface energy / surface area accessible to the electrochemical reaction and (2) crystallinity / crystallographic plane (it could be functional groups in the case of carbon) of the material exposed are quite important. He et al. and Guo et al. have explained the effect of crystallographic plane on the electrocatalytic activities towards oxygen reduction and oxygen evolution reaction.[72,73] the authors have proposed that MnO with (110) facet possesses favourable adsorption energies for oxygen which in turn results in good ORR and OER

In the present studies, the XRD patterns of the three morphologies clearly reveal that wires show diffraction peaks with larger intensities than that observed for the other two morphologies (Fig. 1). The relative intensities of the peaks are very similar though. However, wires are found to be highly crystalline in nature which is reflected in the electron diffraction patterns obtained from microscopy. It should be pointed out that the crystallite size for diffraction is determined to be 319, 331 and 344 Å (± 5Å) for wires, spheres and hexagons respectively. As shown in the reply to the next point, the conductivity for wires are higher than that of other morphologies. Though the sizes are very similar, the surface areas are very different for different morphologies. As mentioned in the manuscript, the available electrochemical surface area is more in the case of wires as compared to other two morphologies. The surface energies are likely to be different as well. Hence, it is suggested that the electrocatalytic activity which is affected by various parameters of combinations of crystallinity, conductivity and surface area / energy is higher for wires than that of other morphologies. Detailed DFT analysis of various morphologies may reveal additional insight in to the activity as a function of morphology.

Hence, it is suggested that the higher catalytic activity observed for 1D morphology is attributed to the following reasons. (1) NiSe wire morphology possesses larger surface area than the other two morphologies based on the capacitance values as described above, thus allowing increased availability and utilization of large number of active sites. (2) The nanowire morphology probably results in fast (unidirectional) electron transport and is exemplified in the next point. The Nyquist plots [Fig. 7(d)] exhibit well-defined semicircles over the high frequency region and the Rct based on the equivalent circuit analysis yields smallest value for NiSe wires (table 2). This is qualitatively observed in the diameter of the semicircle region at high frequencies. Similar arguments have been put forward for Cu_3P and CoP nanowires.[74,75]

Oxygen reduction

ORR is an important reaction that plays a crucial role in fuel cells and metal-air batteries. The linear sweep voltammograms for ORR for NiSe phase, show small variations among different morphologies, with peak potential for wires ~ 25 mV more positive than that of spheres and ~ 50 mV more positive than that of hexagons [Fig. 8(a)]. Similar peak potentials have been reported for other metal chalcogenides (CoSe) and carbon- based materials for ORR.[76,77] The onset potentials also reveal similar trend with -0.18 V for wires and -0.22 V for spheres and -0.23 V for hexagons. The peak currents vary linearly with square root of scan rate indicating diffusion limited reaction. Rotating disk electrode (RDE) measurements have been carried out in the linear sweep mode at a scan rate of 0.005 V s^{-1} in the potential range, -0.1 to -0.7 V. As shown in figure 8(b), the currents increase as a function of rotation rate due to fast mass transport. It is observed that the currents in the region of -0.4 to -0.7 V do not reach saturation limiting value, which is possibly due to residual contributions of mixed mass transfer and kinetic control processes. Similar behavior has been reported in the case of other metal chalcogenides such as $CoSe_2$ towards ORR.[78-80] Various electrochemical kinetic parameters of exchange current density, rate constant, and the number of electrons, are calculated using Koutechy-Levich (K-L) equation as given below.

$$1/i = 1/i_k + 1/i_d$$

$$1/i = -1/(nFkC_o) - 1/(0.62\ nFD_o^{2/3}\upsilon^{-1/6}C_o\omega^{1/2})$$

where i is the current density at different potentials, i_k is kinetic current density, i_d is the diffusion current density, n represents number of electrons transferred per O_2 molecule, k is the rate constant, F is the Faraday constant (96500 C mol^{-1}), D_o is the bulk diffusion co-efficient of O_2 (1.65 X 10^{-6} cm^2 sec^{-1}), C_o is bulk concentration (0.84 X 10^{-6} mole cc^{-1}), ν is kinematic viscosity (0.01 cm^2 sec^{-1}) and ω is rotation speed of the electrode (revolutions sec^{-1}). It should be pointed out that diffusion coefficient of oxygen near the wires / hexagons and spheres of NiSe incorporated in to nafion film and inside the nafion film may be different from that of the bulk value. There may be mixed conditions of diffusion and hence one should be cautious in using the bulk diffusion coefficient value to evaluate the activity of catalysts incorporated in an ionomer film. Figure 10(b) depicts the K-L plots derived from figure 8(a) and linear variation of 1/i with 1/ω at different applied potentials is observed. The slope of 1/j vs $\omega^{-1/2}$ plot gives the number of electrons involved in the reaction and is determined to be 1.7 to 2.3 at different applied potentials for all the morphologies [Fig. 8(b), Table 3]. The reaction seems to terminate at the peroxide stage though there is a continuous increase in currents at more negative potentials, particularly in the case of wires. Intentional spiking of the electrolyte with known concentration of H_2O_2 leads to small increase in currents thus confirming that the peroxide probably do not get reduced further on NiSe phase [Fig. S11]. It is also observed that the reduction of H_2O_2 in N_2 saturated electrolyte does not happen suggesting that NiSe in any morphology is not a very good catalyst for 4 electron process of ORR. Additionally, the loading does not have any effect on the reduction currents. However, it should be pointed out that geometric area is used for the calculations and hence the obtained kinetic parameters are ‘apparent’ values. Effect of presence of methanol is followed by carrying out oxygen reduction in presence and absence of methanol. The i-t transients given in figure 8(c) carried out by spiking methanol in the electrolyte solution does not result in any change suggesting that these materials are inactive towards methanol oxidation. The small spikes observed in the current transients are due to the disturbances during the addition of methanol. Stability of the NiSe towards ORR is checked by carrying out voltammograms for several successive cycles and it is found that [Fig. 8(d)] stable performance is observed even after 1000 cycles with 90-95% retention of initial currents.

Glucose oxidation

It is known that nickel forms hydroxides and oxy-hydroxides in alkaline medium.[70] The oxyhydroxides are catalytically active towards oxidation of glucose. This is very useful in the context of non-enzymatic glucose detection as there is no need to maintain pH of the electrolyte during the experiments. Direct electrochemical oxidation of glucose using nickel selenide is monitored using cyclic voltammetry and chronoamperometry. Oxidation and reduction peaks observed in the cyclic voltammograms of NiSe in the absence of glucose correspond to the $Ni^{2+/3+}$ redox couple. Upon adding glucose, notable enhancement of the oxidation peak current as well as a shift in the anodic peak potential is observed [Fig. 9(a)]. Oxidation of glucose follows the mechanism, involving NiOOH as given below.

$$Ni(OH)_2 + OH^- \longrightarrow NiO(OH) + H_2O + e^-$$

$$NiO(OH) + \text{glucose} \longrightarrow Ni(OH)_2 + \text{glucolactone}$$

Different concentrations of glucose result in increase in anodic currents due to increased formation of Ni (II) species. As reported earlier, the diffusion limitation of the analyte close to the electrode surface is probably responsible for the shift in the anodic peak potential along with the increase in glucose concentration.[47] The chronoamperometric response for successive additions of different concentrations of glucose is given in figure 9(b). The amperometric signals show a linear correlation to glucose concentration [Fig. 9(c)] and the corresponding calibration plot reveals that the sensitivity and minimum detection limit in the case of NiSe wires are good (Fig. S12 and S13). The response time observed in the case of wire morphology is less than 4 sec. while for hexagons and spheres, it is higher (~ 10 sec.). The selectivity of NiSe towards glucose, particularly in presence of interferents such as dopamine, urea and ascorbic acid [Fig. 9(d)] is very good. Table 3 shows the comparison of the parameters for different morphologies of NiSe. Sa and co workers[81] have reported the electro-oxidation of sugars using carbon nanotube modified with nickel oxy-hydroxide electrode in alkaline media. In the present studies, the linearity is observed to up to 3 mmol L^{-1} with detection limit of 5 μmol L^{-1}.

Conclusions

Three different morphologies of NiSe, spheres, hexagons and wires have been achieved by a simple hydrothermal method that involves short preparation time. The nanostructures possess uniform morphologies with good monodispersity. The different selenium precursors result in morphologies that are probably dictated by the by-products as well as relative rates of amorphous selenium formation and dissolution. The semiconducting nature of NiSe is exploited in the photoconductivity measurements that lead to visible light photodetectors. The effect of different morphologies of NiSe on electrochemical hydrogen evolution, oxygen reduction and glucose oxidation has been followed and among the three morphologies, wires are shown to be better than the hexagons and spheres. This is likely to be due to high active surface area, and good electron transport properties due to its one dimensional nature. Additionally, non-enzymatic glucose detection is shown using the wire like morphology of NiSe phase. The different morphologies may manifest in different characteristics in other catalytic and electrocatalytic reactions. This is currently being pursued.

References

1 M. G. Walter, E. L. Warren, J. R. McKone, S. W. Boettcher, Q. Mi, E. A. Santori and N. S. Lewis, *Chem. Rev.*, 2010, **110**, 6446–6473.

2 A. Paracchino, V. Laporte, K. Sivula, M. Graetzel and E. Thimsen, *Nat. Mater.,* 2011, **10**, 456–461.

3 J. A. Turner, *Science*, 2004, **305**, 972-974.

4 N. S. Lewis and D. G. Nocera, *Proc. Natl. Acad. Sci. U. S. A.*, 2006, **103**, 15729–15735.

5 G. J. K. Acres, *Platinum Met. Rev.*, 1984, **28**, 150–157.

6 A. Capon and R. Parsons, *J. Electroanal. Chem.*, 1973, **44**, 239-254.

7 S. M. Alia, K. O. Jensen, B. S. Pivovar and Y. Yan, *ACS Catal.*, 2012, **2**, 858–863.

8 K. Jiang, H.-X. Zhang, S. Zou and W.-B. Cai, *Phys. Chem. Chem. Phys.*, 2014, **16**, 20360–20376.

9 L. A. Kibler, *ChemPhysChem*, 2006, **7**, 985-991.

10 M. M. O. Thotiyl, T. R. Kumar and S. Sampath, *J. Phys. Chem. C*, 2010, **114**, 17934-17941.

11 S.-W. Xie, S. Chen, Z.-Q. Liu and C.-W. Xu, *Int. J. Electrochem. Sci.*, 2011, **6**, 882-888.

12 J. Greeley, I. E. L. Stephens, A. S. Bondarenko, T. P. Johansson, H. A. Hansen, T. F. Jaramillo, J. Rossmeisl, I. Chorkendorff and J. K. Nørskov, *Nat. Chem.*, 2009, **1**, 552-556.

13 J. Greeley, J. K. Nørskov and M. Mavrikakis, *Annu. Rev. Phys. Chem.*, 2002, **53**, 319-348.

14 V. Stamenkovic, B. S. Mun, K. J. Mayrhofer, P. N. Ross, N. M. Markovic, J. Rossmeisl, J. Greeley and J. K. Nørskov, *Angew. Chem., Int. Ed.*, 2006, **45**, 2897-2901.

15 E. Negro, K. Vezzu, F. Bertasi, P. Schiavuta, L. Toniolo, S. Polizzi and V. D. Noto, *ChemElectroChem*, 2014, **1**, 1359-1369.

16 E. Negro, S. Polizzi, K. Vezzu, L. Toniolo, G. Cavinato and V. D. Noto, *Int. J. Hydrogen Energy*, 2014, **39**, 2828–2841.

17 S. Dey and V. K. Jain, *Platinum Met. Rev.*, 2004, **48**, 16-29.

18 J. F. Hull, Y. Himeda, W. H. Wang, B. Hashiguchi, R. Periana, D. J. Szalda, J. T. Muckerman and E. Fujita, *Nat. Chem.*, 2012, **4**, 383–388.

19 V. Artero, M. Chavarot-Kerlidou and M. Fontecave, *Angew. Chem., Int. Ed.,* 2011, **50**, 7238–7266.

20 S. A. Grigoriev, P. Millet and V. N. Fateev, *J. Power Sources,* 2008, **177**, 281–285.

21 M. Neergat, V. Gunasekar and R. Rahul, *J. Electroanal. Chem.*, 2011, **658**, 25–32.

22 E. J. Popczun, J. R. McKone, C. G. Read, A. J. Biacchi, A. M. Wiltrout, N. S. Lewis and R. E. Schaak, *J. Am. Chem. Soc.*, 2013, **135**, 9267–9270.

23 Y. Liu, T. G. Kelly, J. G. Chen and W. E. Mustain, *ACS Catal.*, 2013, **3**, 1184.

24 B. F. Cao, G. M. Veith, J. C. Neuefeind, R. R. Adzic and P. G. Khalifah, *J. Am. Chem. Soc.*, 2013, **135**, 19186–19192.

25 M. S. Faber and S. Jin, *Energy Environ. Sci.*, 2014, **7**, 3519–3542.

26 D.-Y. Wang, M. Gong, H.-L. Chou, C.-J. Pan, H.-A. Chen, Y. Wu, M.-C. Lin, M. Guan, J. Yang, C.-W. Chen, Y.-L. Wang, B.-J. Hwang, C.-C. Chen and H. Dai, *J. Am. Chem. Soc.*, 2015, **137**, 1587−1592.

27 D. Chong, I. P. Georgakaki, M. L. Miller, R. Mejia-Rodriguez and M. Y. Darensbourg, *Dalton Trans.*, 2003, 4158-4163.

28 B. Rauchfuss, *Inorg. Chem.*, 2004, **43**, 14-26.

29 C. Tang, Z. Pu, Q. Liu, A. M. Asiri and X. Sun, *Electrochim. Acta*, 2015, **153**, 508-514.

30 M. S. Faber, M. A. Lukowski, Q. Ding, N. S. Kaiser and S. Jin, *J. Phys. Chem. C*, 2014, **118**, 21347-21356.

31 Q. Liu, J. Shi, J. Hu, A. M. Asiri, Y. Luo and X. Sun, *ACS Appl Mat. Interfaces*, 2015, **7**, 3877-3881.

32 C. Tsai, K. Chan, J. K. Nørskov, and F. Abild-Pedersen, *Cat. Sci. Technol.,* 2015, **5**, 246-253.

33 W. Lubitz, H. Ogata, O. Rudiger and E. Reijerse, *Chem. Rev.*, 2014, **114**, 4081–4148.

34 T. Evans, D. M. Piper, S. C. Kim, S. S. Han, V. Bhat, K. H. Oh and S. H. Lee, *Adv. Mater.*, 2014, **26**, 7386-7392.

35 J. Xu, H. T. Xue, X. Yang, H. X. Wei, W. Y. Li, Z. P. Li, W. J. Zhang and C. S. Lee, *Small*, 2014, **10**, 4754-4759.

36 S. Peng, L. Li, X. Han, W. Sun, M. Srinivasan, S. G. Mhaisalkar, F. Cheng, Q. Yan, J. Chen and S. Ramakrishna, *Angew. Chem., Int. Ed.*, 2014, **53**, 12594-12599.

37 D. Kong, H. Wang, J. J. Cha, M. Pasta, K. J. Koski, J. Yao and Y. Cui, *Nano Lett.*, 2013, **13**, 1341–1347.

38 A. Kratzig, C. Zachaus, S. Brunken, D. Thomas, P. Bogdanoff, K. Ellmer and S. Fiechter, *Phys. Status Solidi* A, 2014, **211**, 2020-2029.

39 C.-W. Su, J.-M. Li, W. Yang and J.-M. Guo, *J. Phys. Chem. C*, 2013, **118**, 767–773.

40 P. Bak, P. Kleban, W. N. Unertl, J. Ochab, G. Akinci, N. C. Bartelt and T. L. Einstein, *Phys. Rev. Lett.,* 1985, **54**, 1539-1542.

41 G. Yue, F. Tan, F. Li, C. Chen, W. Zhang, J. Wu and Q. Li, *Electrochim. Acta*, 2014, **149**, 117-125.

42 H.-J. Kim, S.-W. Kim, C. V. V. M. Gopi, S.-K. Kim, S. Srinivasa Rao and M.-S. Jeong, *J. Power Sources*, 2014, **268**, 163–170.

43 A. Singh, A. J. Roberts, R. C. T. Slade and A. Chandra. *J. Mater. Chem. A,* 2014, **2**, 16723-16730.

44 H. Huo, Y. Zhao and C. Xu, *J. Mater. Chem. A,* 2014, **2**, 15111-15117.

45 T.-W. Lin, C.-J. Liu and C.-S. Dai, *Appl. Catal., B,* 2014, **154**, 213–220.

46 G. Li, H. Huo and C. Xu, *J. Mater. Chem. A*, 2015, **3**, 4922–4930.

47 X. Chen and R. Fan, *Chem. Mater.*, 2001, **13**, 802-805.

48 I. P. Parkin, *Chem. Soc. Rev.*, 1996, **25**, 199-207.

49 J. Zhu, S. T. Aruna, Y. Koltypin and A. Gedanken, *Chem. Mater.*, 2000, **12**, 143–147.

50 J. Zhu, X. Liao, X. Zhao and J. Wang, *Mater. Lett.*, 2001, **47**, 339-343.

51 X. Chen, J. L. Hutchison, P. J. Dobson and G. Wakefield, *J. Colloid Interface Sci.,* 2008, **319**, 140-143.

52 S. Levichev, A. Chahboun, A.G. Rolo, O. Conde and M. J. M. Gomes, *Thin Solid Films*, 2009, **517**, 2538-2540.

53 R. H. Bari and L. A. Patil, *Indian J. Pure Appl. Phys.*, 2010, **48**, 127-132.

54 A. Sobhani, F. Davar and M. Salavati-Niasari, *Appl. Surf. Sci.*, 2011, **257**, 7982–7987.

55 M. A. Hines and P. Guyot-Sionnest, *J. Phys. Chem.*, 1996, **100**, 468–471.

56 W. M. Du, X. F. Qian, X. S. Niu and Q. Gong, *Cryst. Growth. Des.*, 2007, **7**, 2733-2737.

57 K. Anuar, Z. Zainal, N. Saravanan and A. R. Kartini, *AJSTD,* 2004, **21**, 19-25.

58 J. T. Hu, T. W. Odom and C. M. Lieber, *Acc. Chem. Res.*, 1999, **32**, 435-445.

59 R. Liu and S. B. Lee, *J. Am. Chem. Soc.*, 2008, **130**, 2942-2943.

60 A. Pan, S. Wang, R. Liu, C. Li and B. Zou, *Small*, 2005, **1**, 1058–1062.

61 M. R. Gao, Z. Y. Lin, T. T. Zhuang, J. Jiang, Y. F. Xu, Y. R. Zheng and S. H. Yu, *J. Mater. Chem.*, 2012, **22**, 13662–13668.

62 F. Gong, H. Wang, X. Xu, G. Zhou and Z. S. Wang, *J. Am. Chem. Soc.*, 2012, **134**, 10953–10958.

63 Z. B. Zhuang, Q. Peng, J. Zhuang, X. Wang and Y. D. Li, *Chem.–Eur. J.*, 2006, **12**, 211–217.

64 Q. Peng, Y. J. Dong, Z. X. Deng, H. Z. Kou, S. Gao and Y. Li, *J. Phys. Chem. B*, 2002, **106**, 9261-9265.

65 Q. Peng, Y. J. Dong and Y. Li, *Angew. Chem., Int. Ed.,* 2003, **42**, 3027–3030.

66 U. Jeong and Y. Xia, *Adv. Mater.*, 2005, **17**, 102-106.

67 W. D. Shi, X. Zhang and G. B. Che, *Int. J. Hydrogen Energy,* 2013, **38**, 7037-7045.

68 W. J. Liang, O. Rabin, A. I. Hochbaum, M. Fardy, M. J. Zhang and P. D. Yang, *Nano Res.*, 2009, **2**, 394–399.

69 R. J. Mehta, C. Karthik, W. Jiang, B. Singh, Y. Shi, R. W. Siegel, T. Borca-Tasciuc and G. Ramanath, *Nano Lett.*, 2010, **10**, 4417–4422.

70 D. T. Schoen, C. Xie and Y. Cui, *J. Am. Chem. Soc*., 2007, **129**, 4116-4117.

71 P. P. Hankare, B. V. Jadhav, K. M. Garadkar, P. A. Chate, I. S. Mulla and S. D. Delekar, *J. Alloys Compd.*, 2010, **490**, 228–231.

72 C.-H. Kuo, I. M. Mosa, S. Thanneeru, V. Sharma, L. Zhang, S. Biswas, M. Aindow, S. P. Alpay, J. F. Rusling, S. L. Suib and J. He, *Chem. Commun.*, 2015, **51**, 5951-5954.

73 . Xiao, Q. Kuang, S. Yang, F. Xiao, S. Wang and L. Guo, *Sci. Rep.*, 2013, **3**, 2300.

74 P. Jiang, Q. Liu, C. Ge, W. Cui, Z. Pu, A. M. Asiri and X. Sun, *J. Mater. Chem. A,* 2014, **2**, 14634–14640.

75 J. Q. Tian, Q. Liu, N. Y. Cheng, A. M. Asiri and X. P. Sun, *Angew. Chem., Int. Ed.*, 2014, **53**, 9577–9581.

76 Y. Gorlin, C.-J. Chung, D. Nordlund, B. M. Clemens and T. F. Jaramillo, *ACS Catal.*, 2012, **2**, 2687–2694.

77 D. Wang, X. Chen, D. G. Evans and W. Yang, *Nanoscale,* 2013, **5**, 5312–5315.

78 M. R. Gao, S. Liu, J. Jiang, C. H. Cui, W. T. Yao and S. H. Yu, *J. Mater. Chem.*, 2010, **20**, 9355–9361.

79 D. Susac, L. Zhu, M. Teo, A. Sode, K. C. Wong, P. C. Wong, R. R. Parsons, D. Bizzotto, K. A. R. Mitchell and S. A. Campbell, *J. Phys. Chem. C*, 2007, **111**, 18715–18723.

80 A. M. Ghonim, B. E. El-Anadoulin and M. M. Saleh, *Electrochim. Acta*, 2013, **114,** 713–719.

81 A. C. Sa, L. L. Paim and N. R. Stradiotto, *Int. J. Electrochem. Sci.*, 2014, **9**, 7746−7762.

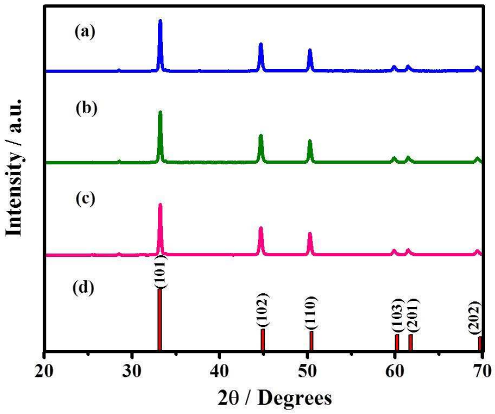

Fig. 1 Powder X-ray diffraction patterns of (a) NiSe wires, (b) NiSe spheres and (c) NiSe hexagons prepared using 1:3 mole ratio of $NiCl_2.6H_2O$ and selenium precursors (selenourea, SeO_2 and KSeCN) at 180°C for 8 h and (d) standard reference pattern of NiSe (JCPDS # 18-0888).

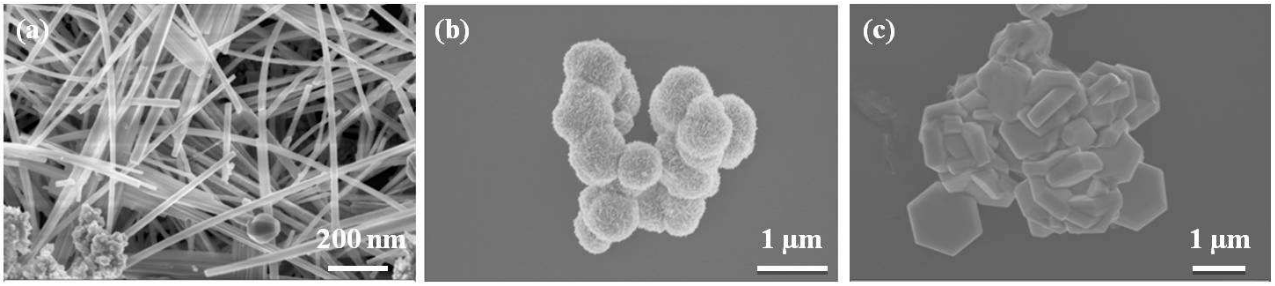

Fig. 2 Scanning electron microscopy images of (a) NiSe wires, (b) NiSe spheres and (c) NiSe hexagons.

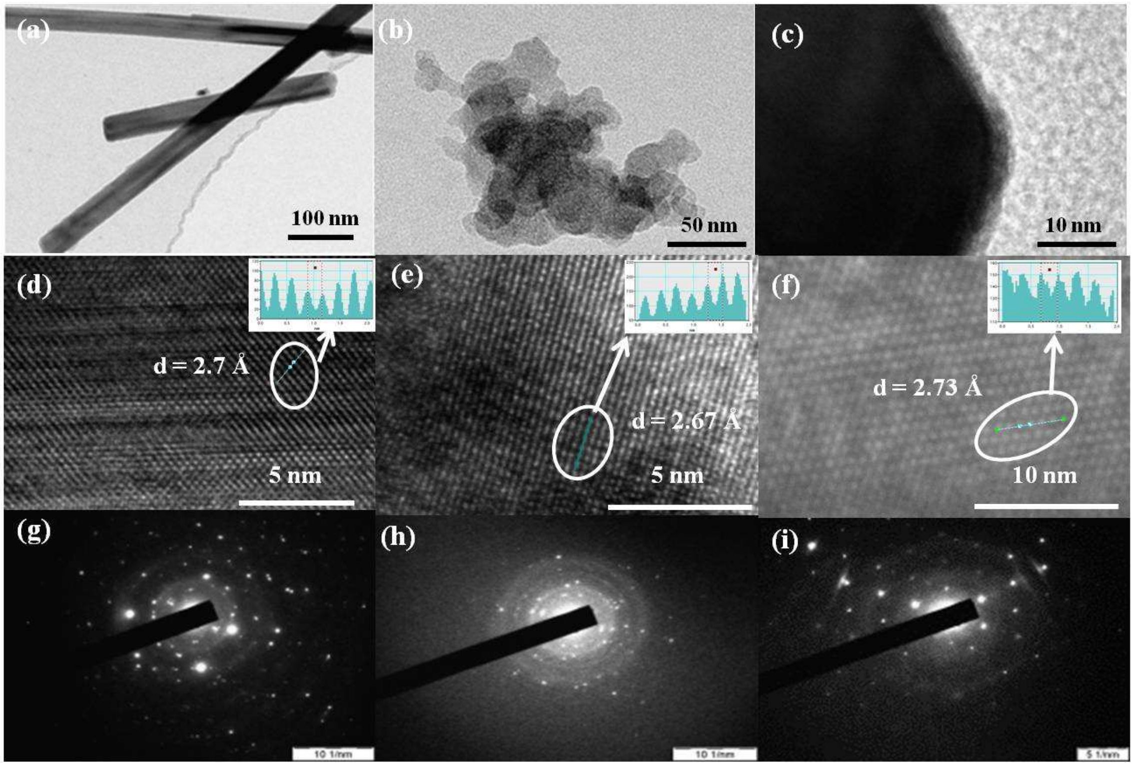

Fig. 3 Transmission electron microscopy images of (a) NiSe wires, (b) NiSe spheres and (c) NiSe hexagons and (d) to (f) are high resolution TEM images of wires, spheres and hexagons (insets are the corresponding intensity line profiles) and (g) to (i) represent the SAED patterns of the corresponding morphologies.

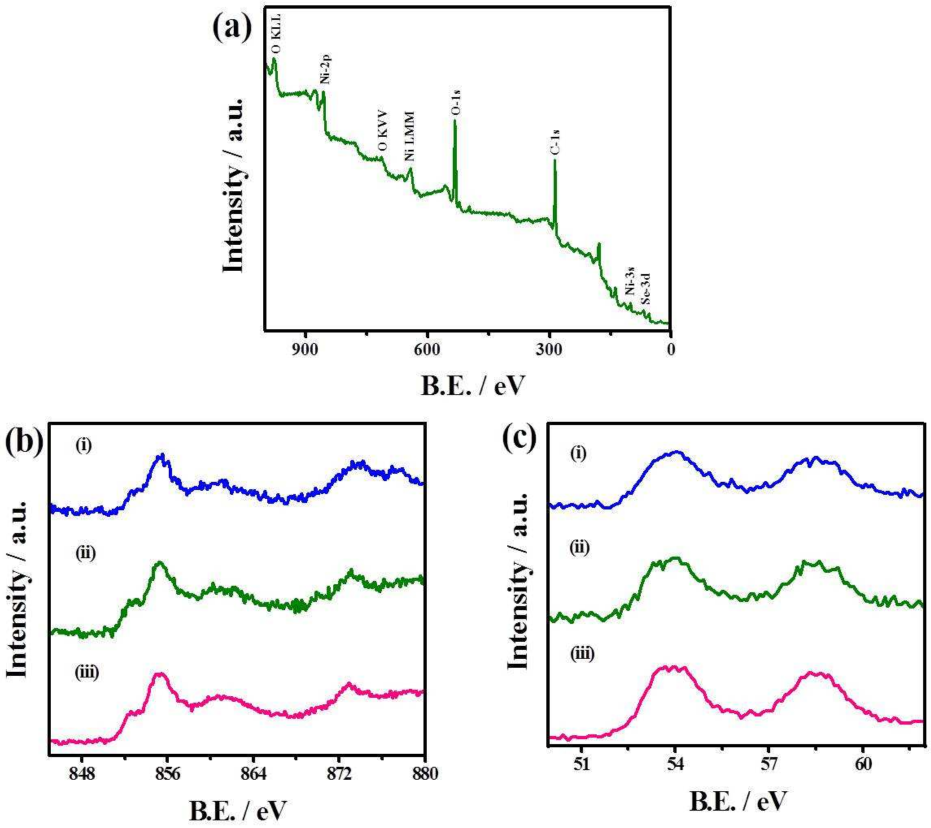

Fig. 4 X-ray photoelectron spectra of different morphologies of NiSe phase (a) survey spectrum of nanowires, (b) high resolution spectra of Ni-2p and (c) Se-3d regions in the case of (i) wires, (ii) spheres and (iii) hexagons.

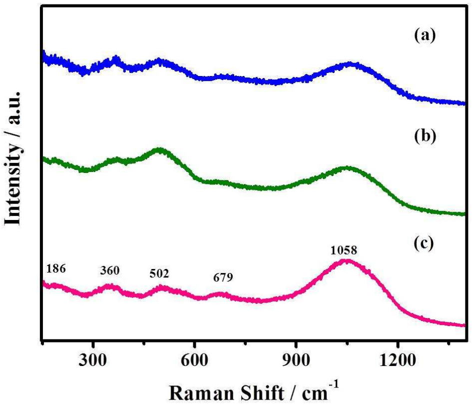

Fig. 5 Raman spectra of NiSe phase (a) wires, (b) spheres and (c) hexagons. Laser wavelength of 514.7 nm is used.

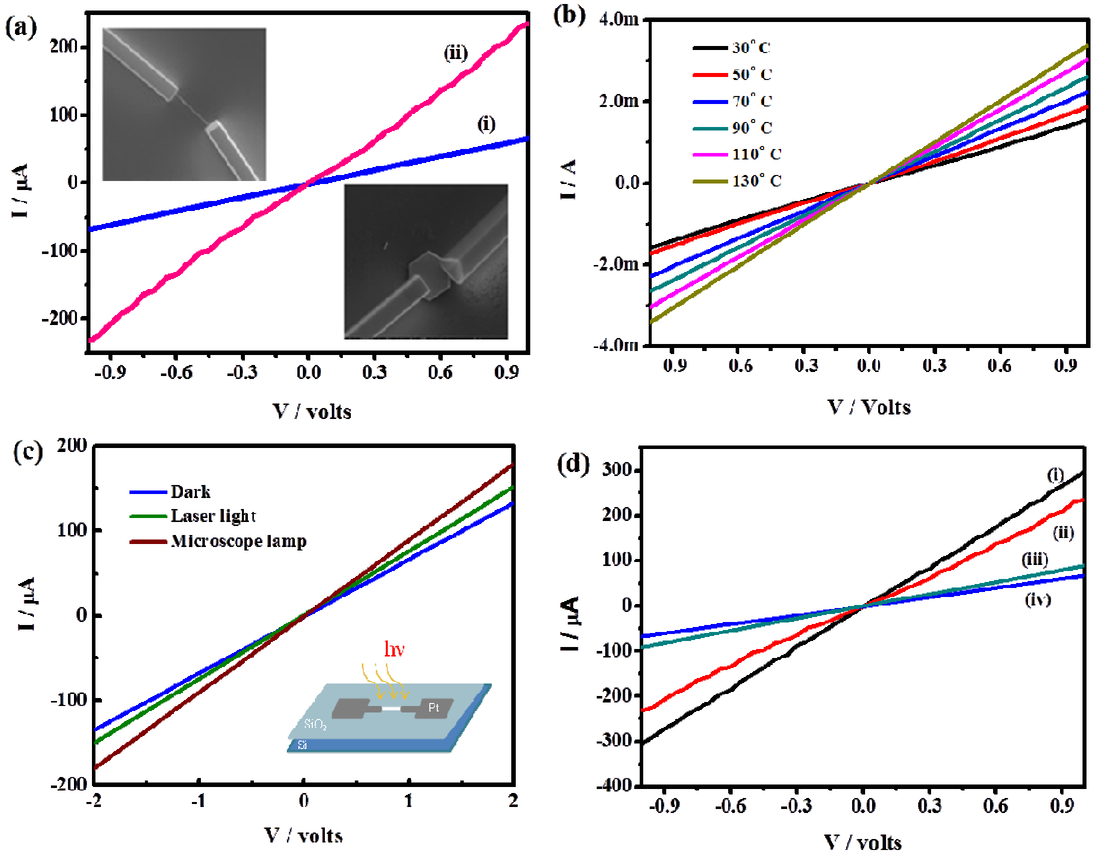

Fig. 6 *I-V* characteristics of (a) single NiSe nanowire (i) and NiSe hexagon (ii) (inset SEM image (scale bar 5 µm) with Pt contacts given by FIB) and (b) effect of variation of temperature on bundle of NiSe wires (temperature is increased in the increments of 20^{o}C, from 30°C to 130°C), (c) Photoresponse of NiSe wire in dark and in the presence of laser light (red laser) and microscope lamp at room temperature (d) comparison of photoresponses of NiSe wire (iii) and (iv); hexagon (i) and (ii) - based devices: (ii) and (iv) dark; (i) and (iii) in the presence of microscope lamp.

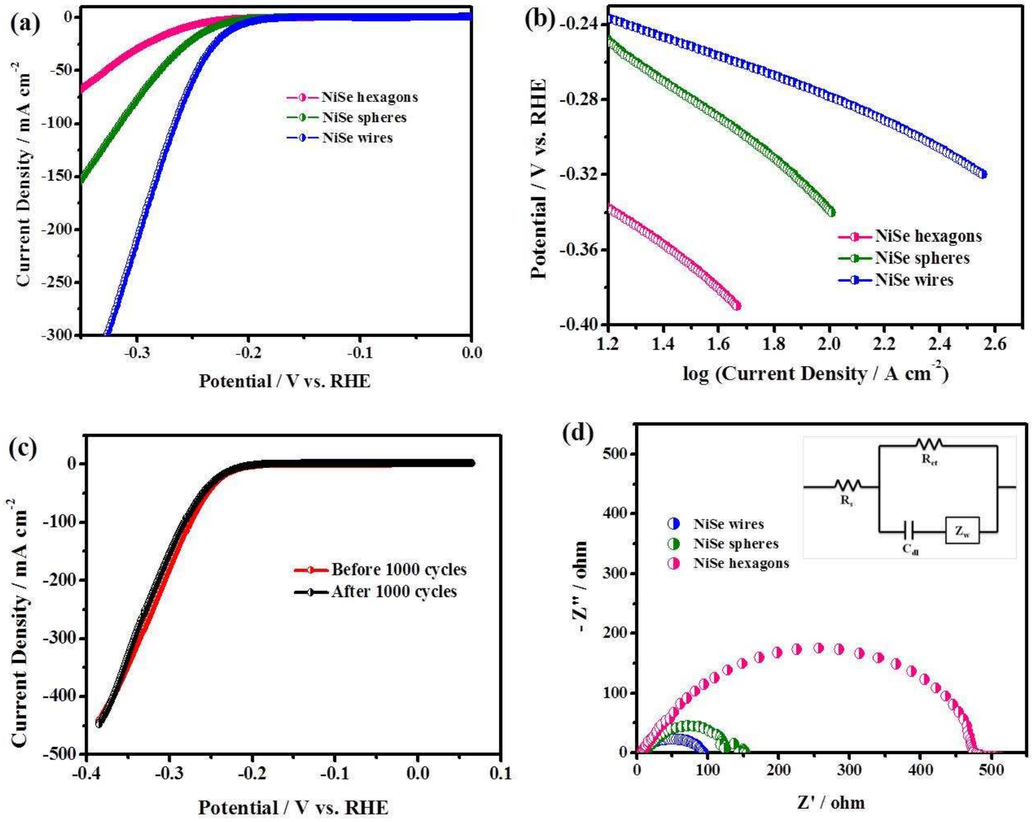

Fig. 7 (a) Linear polarization curves obtained with different morphologies of NiSe (given in the figures); (b) corresponding Tafel-plots for a catalyst loading of 0.56 mg/cm^2. (c) Linear sweep voltammograms for the NiSe nanowires catalyst (before and after 1000 cycles). (d) Electrochemical impedance spectra of wires, spheres and hexagons obtained with a AC amplitude of 5 mV at a DC bias of -0.235 V (inset gives the equivalent circuit used).

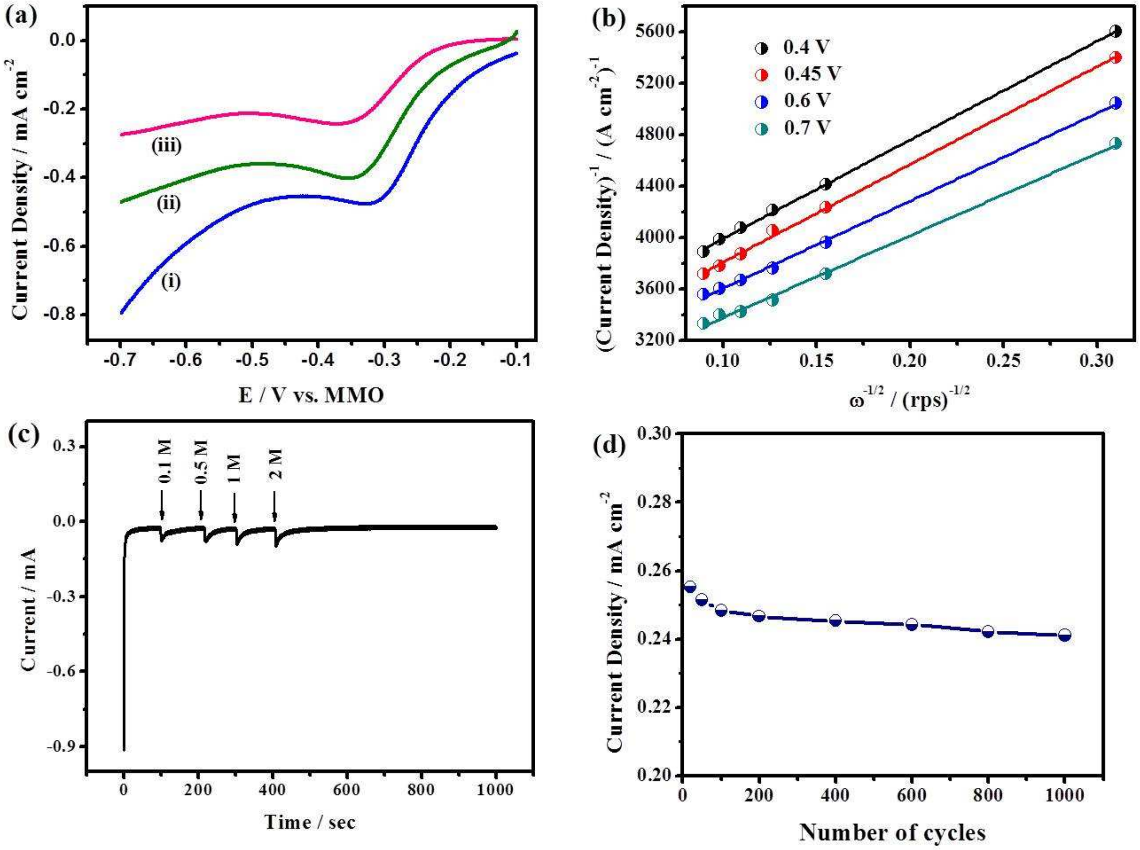

Fig. 8 (a) Linear sweep voltammograms on (i) NiSe wires, (ii) spheres and (iii) hexagons in presence of O_2 saturated solution of 0.1 mol L^{-1} KOH at a scan rate of 2 mV s^{-1}. (b) Koutecky-Levich plots for NiSe nanowires at different potentials. (c) Chronoamperometric curve at a potential of -0.4 V with addition of different concentrations of methanol. (d) Stability of the NiSe nanowires (current density at the peak potential) for different number of cycles.

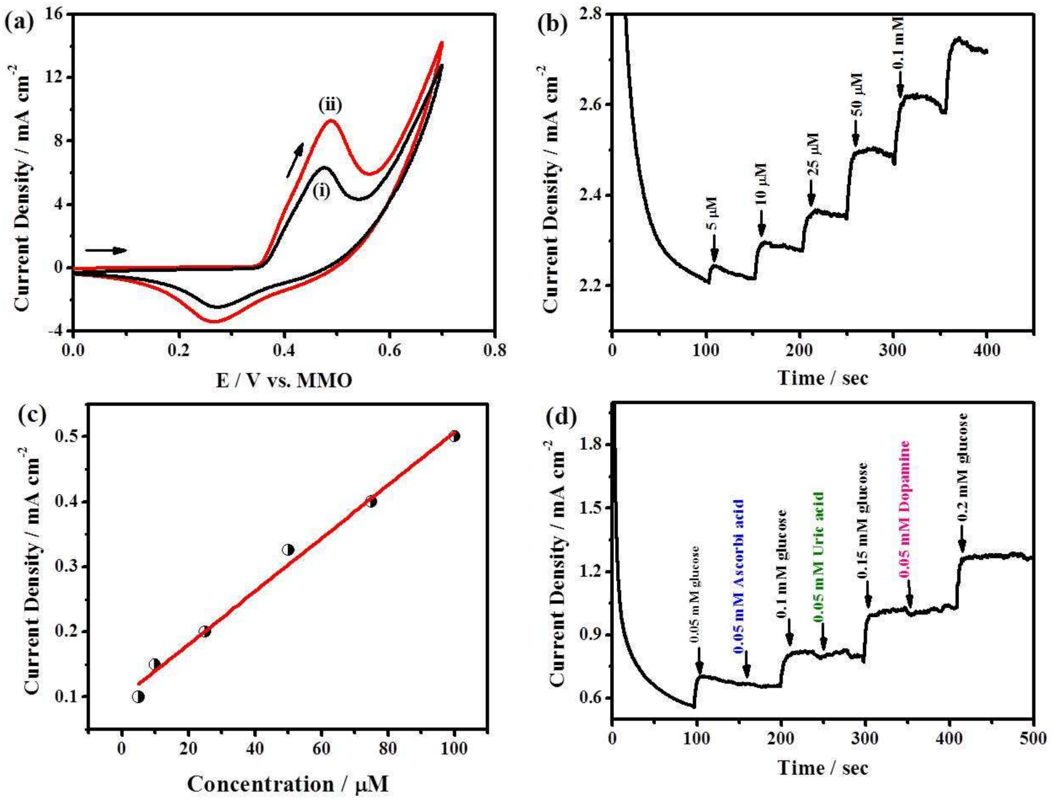

Fig. 9 (a) Cyclic voltammograms on NiSe nanowires in 0.5 mol L^{-1} aqueous NaOH in the (i) absence and (ii) presence of 0.5 mmol L^{-1} glucose, at a scan rate of 20 mV s^{-1} (b) amperometric response of NiSe nanowires on GC electrode with successive additions of glucose at potential 0.5 V. (c) corresponding calibration curve. (d) current response to successive additions of 0.05 mmol L^{-1} glucose, 0.05 mmol L^{-1} ascorbic acid, 0.05 mmol L^{-1} uric acid, 0.05 dopamine in 0.5 mol L^{-1} NaOH at 0.45 V.

Table 1. Basic electrochemical parameters obtained for NiSe in presence of 10 mmol L^{-1} $K_4[Fe(CN)_6]$ in 0.1 mol L^{-1} KCl. E_f^0, $E_{pp,}$ i_c / i_A represent formal potential (average of cathodic and anodic peak potentials), peak to peak separation and cathodic / anodic peak currents respectively.

Material morphology	E_f^0 (mV)	E_{pp} (mV)	i_c / i_A
NiSe wires	475	58	0.94
NiSe spheres	428	136	0.87
NiSe hexagons	435	123	0.69

Table 2. Electrochemical parameters obtained from impedance spectra for different morphologies of NiSe, in presence of 0.5 mol L^{-1} H_2SO_4 electrolyte saturated with nitrogen. R_s, R_{ct} and C_{dl} correspond to solution resistance, charge transfer resistance and double layer capacitance respectively. W represent Warburg exponent.

Morphology	R_s (Ω)	R_{CT} (Ω)	C_{dl} (mF)	W
NiSe wires	8.4	92.6	1.6	0.012
NiSe spheres	8.3	131	2.1	0.007
NiSe hexagons	6	461	1.6	0.002

Table 3. Comparison of the parameters obtained for glucose detection on different morphologies of NiSe.

Morphology of NiSe	**Sensitivity** (μ**A mM^{-1} cm^{-2}**)	**Linear range** (**mmol L^{-1}**)	**Minimum detection limit** (**μmol L^{-1}**)
Wires	4080	0.005 – 3	5
Spheres	3280	0.005 – 3	5
Hexagons	2750	0.005 – 3	5